Antimicrobial activity of TiO$_2$:Ag nanocrystalline heterostructures: Experimental and theoretical insights

Rafaela S. André [a], Camila A. Zamperini [b], Ewerton G. Mima [c], Valéria M. Longo [d,*], Anderson R. Albuquerque [e,f], Júlio R. Sambrano [e], Ana L. Machado [c], Carlos E. Vergani [c], Antonio C. Hernandes [d], José A. Varela [b], Elson Longo [b]

[a] UFSCar – Universidade Federal de São Carlos, Department of Chemistry, 13565-905 São Carlos, SP, Brazil
[b] UNESP – Universidade Estadual Paulista, Instituto de Química, 14801-907 Araraquara, SP, Brazil
[c] UNESP – Universidade Estadual Paulista, Escola de Odontologia de Araraquara, Departamento de Materias Odontológicos e Próteses Dentárias, 14801-903 Araraquara, SP, Brazil
[d] USP – Universidade de São Paulo, Instituto de Física de São Carlos, 13560-970 São Carlos, SP, Brazil
[e] UNESP – Universidade Estadual Paulista, Grupo de Modelagem e Simulação Molecular, P.O. Box 477, CEP 17033-360 Bauru, SP, Brazil
[f] Instituto Federal de Educação, Ciência e Tecnologia do Sertão Pernambucano, IFSetão-PE, 56400-000 Floresta, PE, Brazil

ARTICLE INFO

ABSTRACT

We report the synthesis and characterization of silver-decorated titanium dioxide (TiO$_2$:Ag) nanoparticles, as well as a discussion of their antimicrobial activity. This material was synthesized by microwave-assisted hydrothermal treatment and characterized by complementary techniques. The minimum inhibitory concentration and minimum bactericidal/fungicidal concentration of TiO$_2$:Ag nanoparticles against planktonic and biofilm-forming strains of methicillin-resistant *Staphylococcus aureus*, *Candida* species (spp.) and the total biofilm mass were determined. The basis of the biological activity of TiO$_2$:Ag was investigated by electronic analysis of the material using theoretical quantum chemical calculations. In the proposed mechanism of action, the impregnated semiconductor donates electrons to the forbidden band gaps in the metal, generating point defects, with partially located electrons and holes at the surface, initiating a radical process involving the solvent and biological target. Our results suggest that this TiO$_2$:Ag nanomaterial has potential for use in the development of new therapeutic agents.

© 2015 Elsevier B.V. All rights reserved.

1. Introduction

Nanocrystalline titanium dioxide (nc-TiO$_2$) is a modern photoactive material with a wide range of possible applications, such as in solar cells, self-cleaning fibers, pollutant removal [1], sunscreen [2], water splitting, and as an antifungal agent via photokilling [3–7]. Desirable characteristics exhibited by nc-TiO$_2$ include stability, nontoxicity, chemical inertness, low cost, as well as antimicrobial activity. TiO$_2$ nanoparticles can be designed in crystalline form, with the rutile and anatase phases being the most stable. To improve its antimicrobial properties, modifications of TiO$_2$ have been proposed, such as the addition of noble metal dopants [8].

Silver (Ag) is the most extensively studied nanoparticle used for microbial inactivation, and its antimicrobial efficacy has been attributed to the release of ions and/or production of reactive oxygen species (ROS) [9]. When TiO$_2$ is modified by Ag addition, the Ag can also contribute to antimicrobial activity, by interacting with either proteins in the bacterial cell membrane or intracellular elements such as DNA, leading to cell death [10].

The yeast, *Candida albicans*, an opportunistic commensal of humans, can cause infections when favorable alterations occur in the local or systemic environment, such as with the use of dentures or immunosuppressive agents. Infections caused by *C. albicans* range from superficial, mucosal infections to systemic, life-threatening diseases. Although *C. albicans* is the most prevalent and virulent species, other species from this genus have also been isolated from candidal infections, such as *C. glabrata* and *C. tropicalis* [11]. The increasing prevalence of infections caused by non-albicans *Candida* spp. is significant, as these infections may be intrinsically resistant to antifungal agents, with mortality rates similar to that observed for *C. albicans* infection [12].

Overuse and misuse of antibiotics have led to the emergence of multidrug-resistant bacterial strains. Methicillin-resistant *Staphylococcus aureus* (MRSA) is a major human pathogen, often causing nosocomial infections. Recently, the emergence of community-associated MRSA has also been a matter of serious concern because it

can cause widespread and/or severe disease in an otherwise healthy population [13]. The ability of MRSA to grow on host surfaces and biomaterials used in indwelling medical devices is an important virulence factor frequently associated with chronic/recurrent infections. Therefore, there is an urgent need to develop new antibacterial agents. Nanomaterials offer an attractive alternative to antimicrobial agents and have drawn considerable research interest in the biological field.

The development of heterostructured nanomaterials with novel capacities for recombination of electrons and holes in the band gap is considered a good approach to combating microbial resistance. Although several approaches have been reported for combining nanomaterials, there is a need to optimize the resultant structure as well as its microstructure. In this context, hydrothermal treatment assisted by microwave irradiation (HTMW) is a safe, eco-friendly, and reproducible method, which is widely used for synthesizing various nanomaterials [14].

Biofilms are structured communities of microbial cells attached to a surface enclosed in a self-produced, complex, biopolymer matrix. Cells in biofilms are phenotypically distinct from their planktonic forms, and exhibit increased resistance to antimicrobial drugs and host defense mechanisms [15]. Although biofilm formation is the most common mode of microbial survival in a natural ecosystem, to the best of our knowledge, there are no reported studies to date evaluating the effect of TiO_2 nanoparticles decorated with Ag (TiO_2:Ag), obtained by HTMW, on *Candida* spp. and MRSA biofilms.

Therefore, the goals of this study were to synthesize TiO_2:Ag by using HTMW and to assess the antimicrobial activity of this nanomaterial against *Candida* spp. and MRSA. Due to difficulties in assigning correct electronic responses at atomistic resolution, the key factor governing the antifungal activity of nc-TiO_2 is still unclear. Fortunately, first-principle simulations can fundamentally extend our understanding of electronic properties at atomic-scale resolution. Therefore, to complement experimental data, the bulk of the anatase and metallic Ag in TiO_2:Ag was evaluated by first-principle calculations. In light of these results, an antifungal mechanism, involving the formation of ROS, was formulated.

2. Experimental section

2.1. Preparation and characterization of TiO_2:Ag

To obtain nanoparticles of TiO_2, titanium isopropoxide ($Ti[OCH(CH_3)_2]_4$) with 97% purity, sourced from Alfa Aesar, was used as a precursor of titanium (Ti) in isopropanol. A solution of the Ti in isopropanol was prepared to a final concentration of 0.0025 M Ti, and hydrolysis was performed with an excess of H_2O:Ti of 500:1. The solution was maintained under constant agitation in an ice bath. The white colloid was placed in a sealed 100-mL Teflon autoclave and HTMW was applied by using 2.45-GHz microwave radiation at 800-W power. The sample was heated at 140 °C for 16 min, resulting in a white precipitate; then, the autoclave was naturally cooled to room temperature. The product was washed until the pH reached 7 and dried in an oven at 100 °C. For Ag impregnation, the TiO_2 obtained was suspended in distilled water (9 wt% solid loading), and the pH was adjusted to 5 with HNO_3. While the solution was constantly stirred at 60 °C, 5 mL of $AgNO_3$ (1.4×10^{-2} M) and NaOH were added to raise the pH to 9, resulting in a brown precipitate [16]. The precipitate was washed until the pH reached 7, and then dried in an oven. An aqueous solution of the resultant TiO_2:Ag (2000 mg L^{-1}) was prepared for microbiological testing.

TiO_2:Ag nanostructures were characterized by X-ray diffraction (XRD), carried out on the as-prepared sample using a Rigaku DMax 2500PC diffractometer at 40 kV and 150 mA with Cu-Kα radiation, a graphite monochromator, and a rotary anode, as well as by high-resolution transmission electron microscopy (HRTEM); Tecnai G2TF20, FEI. Morphological and size characterization were performed by field-emission gun scanning electron microscopy (FEG-SEM; Supra 35-VP, Carl Zeiss). Raman spectra at room temperature were obtained using a Horiba Jobin–Yvon Raman LabRAM microspectrometer with 514 nm as the excitation wavelength, through an Olympus TM BX41 microscope. The Cary 5G spectrometer was used to measure ultraviolet–visible (UV–vis) absorption in order to calculate the energy of the band gap. To better understand the characterization of TiO_2:Ag, the short-range order of pure TiO_2 was investigated by Fourier transform (FT)-Raman analysis and UV–vis absorption.

2.2. Procedure for determining antimicrobial activity

To determine the antimicrobial effect of the TiO_2:Ag solution synthesized, the minimum inhibitory concentration (MIC) of planktonic cells and the minimum bactericidal concentration (MBC)/fungicidal concentration (MFC) of planktonic cells and also biofilm-forming cells (MBCb/MFCb) were determined using a broth microdilution assay, as described by the Clinical and Laboratory Standards Institute [17,18] (documents M7-A7 and M27-A3), with some modifications. Standard strains of MRSA, *C. albicans*, *C. glabrata*, and *C. tropicalis* from the American Type Culture Collection (ATCC 33591, ATCC 90028, ATCC 2001, and ATCC 4563, respectively) were used. In all subsequent procedures, unless otherwise specified, tryptic soy broth (Acumedia Manufacturers, Inc.) and RPMI-1640 medium (Sigma–Aldrich) were used for MRSA and *Candida* spp., respectively. The solid media used were mannitol salt agar (Acumedia Manufacturers, Inc.) for MRSA and Sabouraud dextrose agar (Acumedia Manufacturers Inc.) containing 5 μg mL^{-1} gentamicin for *Candida* spp. To prepare the inoculum, *Candida* spp. and MRSA were individually streaked onto agar medium and incubated for 48 h at 37 °C. One loopful of each culture was individually transferred to 10 mL of broth and incubated overnight at 37 °C in an orbital shaker set at 75 rpm. The microbial cells were then harvested by centrifugation at $4000\times$ *g* for 5 min, washed twice with phosphate-buffered saline (PBS; pH 7.2), and resuspended in their respective media.

The MIC and MBC/MFC were determined by incubating MRSA and *Candida* spp., individually, in 96-well microtiter plates for 24 h at 37 °C, while being exposed to serial two-fold dilutions of TiO_2:Ag solution (from 1000 mg L^{-1} to 15.62 mg L^{-1}) in their respective media. Inoculated broth without TiO_2:Ag solution was used as the positive control and uninoculated broth was used as the negative control. The MIC was defined as the lowest concentration of TiO_2:Ag at which no microbial growth was detected by visual inspection. To establish the MBC/MFC, 10-μL aliquots from each well were inoculated in duplicate onto agar plates. After 48 h of incubation at 37 °C, the number of colony-forming units per milliliter (CFU mL^{-1}) was counted and the $\log_{10}$(CFU mL^{-1}) value was calculated. The MBC/MFC was defined as the lowest concentration of TiO_2:Ag solution resulting in no detectable growth.

To determine the MBCb/MFCb and the total biomass of mature 48-h biofilms, the colonies were quantified (CFU mL^{-1}) and the absorbance of the crystal violet stain was determined. Spectrophotometrically standardized cell suspensions (MRSA: 1×10^7 cells mL^{-1}; *Candida* spp.: 1×10^6 cells mL^{-1}) were placed into each well of 96-well microtiter plates and incubated for 90 min at 37 °C in an orbital shaker set at 75 rpm; this was the cell-adhesion phase. The wells were then washed twice with 200 μL of PBS to remove non-adherent cells and filled with 200 μL of the broth medium, and the plates were incubated again (37 °C, 75 rpm, 48 h). The broth medium was replaced with 100 μL of fresh

medium after 24 h. Following biofilm formation (48 h), the medium was aspirated, and non-adherent cells were removed by washing twice with 200 μL of PBS. Broth medium (200 μL) containing various concentrations (from 1000 mg L^{-1} to 15.62 mg L^{-1}) of TiO$_2$:Ag was added to the biofilms, followed by incubation for 24 h. To determine the MBCb/MFCb, the biofilms were scraped out of the wells and suspended in 1000 μL of PBS with vigorous vortex mixing for 1 min. For the contents of each well, 10-fold dilutions were prepared, and 10-μL aliquots of these were inoculated in duplicate on agar plates. After 48 h of incubation at 37 °C, the CFU mL^{-1} value was determined and the log$_{10}$(CFU mL^{-1}) value was calculated. For the determination of total biomass, biofilms were fixed with methanol and stained with 1% crystal violet solution for 5 min. The stain bound to the biofilm was dissolved in 33% acetic acid solution and the optical density was measured at 570 nm using a spectrophotometer (Thermo Plate TP-Reader). For experiments involving both planktonic and biofilm-forming cells, cells incubated in broth medium without TiO$_2$:Ag were used as the positive control, while plain broth medium (without cells or TiO$_2$:Ag) was used as the negative control. All experiments were performed in triplicate on three independent occasions. Data obtained from CFU mL^{-1} and total biomass quantifications were statistically assayed by analysis of variance and Tukey's post hoc test at 5% significance.

3. Computational method and models

To determine the electronic effects of the metal/oxide heterostructure on biological activity, we conducted a computational simulation of anatase-phase TiO$_2$ and Ag by using a periodic approach of density functional theory. The anatase phase of TiO$_2$ has a tetragonal structure belonging to the $I4_1/amd$ space group, defined by two lattice parameters (a = 3.78 Å and c = 9.51 Å), and one internal coordinate, u = 0.208. The Ag unit cell is a cubic hexoctahedron (Fm_3m space group), composed of a single non-equivalent atom with the lattice parameters $a = b = c$ = 4.04 Å. We have previously studied this system and used this computational methodology for several conditions, including surfaces [19,20], point defects [21], and bulk disorder [22].

Besides the separated computational simulation for metal and oxides be sufficient to explain the electronic band alignment for extended systems [23–25], we presented also a more realistic structural model for nano heterostructure. This model was built by supporting a neutral [Ag$_4$] cluster on the periodic 2 × 2 (1 0 1) TiO$_2$ surface supercell (the most stable titanium dioxide surface) [20] with one oxygen vacancy at the topmost O atom. The computational study of metal clusters on a supporting oxide surface presents a large number of almost degenerated isomers. The number of possible stable configurations with several cluster size to find the global minimum is not a trivial task, so is outside of the scope and aim of the present work. Small clusters are useful models to access the most important properties related to metal/support interaction. So, the present model does possible to clarify the electron transfer and charge accumulation around the clusters and include all point defects discussed here. Theoretical models with increasing amount of supported Ag atoms will converge the electronic properties toward the separated systems. So, the proposed [Ag]$_4$/TiO$_{2-x}$ model is the minimum one to explain the main features of this material.

All simulations were carried out using the CRYSTAL14 [26] computer code with the HSE06 Heyd–Scuseria–Ernzerhof exchange–correlation functional [27]. CRYSTAL uses a Gaussian-type basis set to represent crystalline orbitals as a linear combination of Bloch functions defined in terms of local functions (atomic orbitals). The atomic centers were treated using the all-electron Gaussian-type

basis set (s/sp/d): Ti 6/6621/31, O 6/31/1, and Ag 6333/53211/531. Diagonalization of the Fock matrix was performed using the Monkhorst–Pack grid with 16 k-points for Ag and 30 k-points for TiO$_2$. The accuracy of the Coulomb and exchange series was controlled by a set of five thresholds (10^{-8}, 10^{-8}, 10^{-8}, 10^{-8}, and 10^{-18}).

The atomic positions of all atoms in all models were fully relaxed until the largest component of the ionic forces was <3 × 10^{-4} eV/Å. The electronic structure, density of states (DOS) and band structure were analyzed using the Properties14 module in CRYSTAL, employing the same k-points sampling as the diagonalization of the Fock matrix for optimization of the data.

4. Results and discussion

TiO$_2$ and TiO$_2$:Ag samples were characterized with respect to their long-range order from XRD patterns. As shown in Fig. 1, samples of both TiO$_2$ and TiO$_2$:Ag were indexed as the anatase phase of TiO$_2$ with tetragonal structure (powder diffraction file [PDF] number 21-1272). Diffraction peaks related to secondary phases were detected and indexed as metallic Ag (Ag; PDF number 65-2871), in addition to the primary anatase phase of TiO$_2$, in the TiO$_2$:Ag sample.

These results show the anatase phase of the nanomaterial has broad peaks; these are an indication of the structural disorder of the nanomaterial [24], which is a consequence of the synthesis method. HTMW is an economical and quick method to obtain crystalline structures. Several highly crystalline materials with nanoassembled morphology have previously been obtained using this method of synthesis [28,29]. The results of Rietveld analysis of well-ordered nanoparticles, formed with the assistance of HTMW, highlight the changes in their intermediate-range order, which generate freezing distortion of the angles between the clusters constituents of crystalline structure [28,30]. These distortions and tilts are important in the formation of hole–electron pairs and their final recombination in semiconductors [24,31]. In particular, in TiO$_2$:Ag, there is a surface modification attributed to the misalignment between the TiO$_2$ and metallic Ag phases. X-rays interact with several planes of the material, and, consequently, the diffraction pattern is typical of bulk analysis, resulting from various diffraction planes. In the case of our as-prepared sample, TiO$_2$ recovered by metallic Ag, long-range analysis detected modifications identified by metallic Ag peaks on the TiO$_2$ surface.
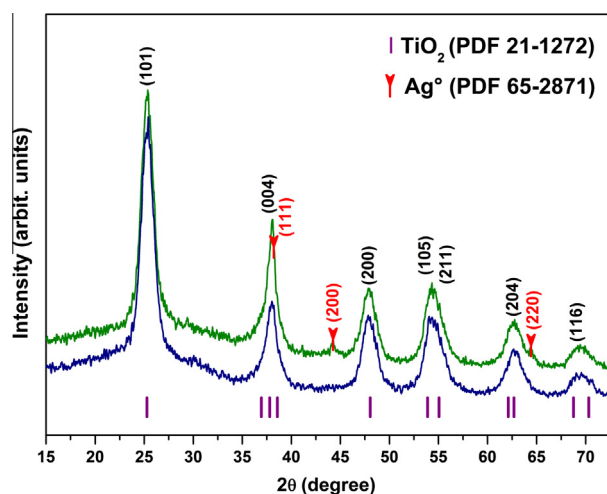

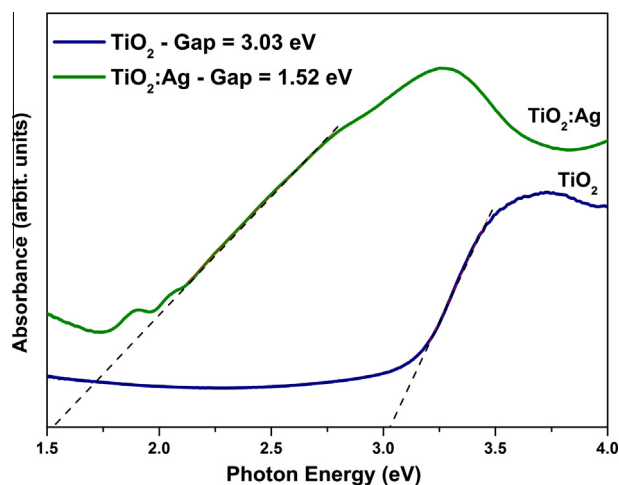Fig. 1. X-ray diffraction patterns of TiO$_2$ (anatase phase; PDF number 21-1272) and TiO$_2$:Ag.

Fig. 2. UV–visible absorption spectra for TiO_2 and TiO_2:Ag samples.

Fig. 3. Band structure and projected density of states. (a) Ag and (b) TiO_2; the TiO_2:Ag heterostructure.

The experimental spectral dependence of absorbance of the sample prepared by the co-precipitation method and HTMW is depicted in Fig. 2.

The optical energy band gap is related to absorbance and photon energy through the following equation, previously described by Wood and Tauc [32]:

$$h\upsilon\alpha \propto (h\upsilon - E_g^{opt})^2$$

where α is the absorbance, h is the Planck constant, ν is the frequency, and E_g^{opt} denotes the optical band gap.

The optical band gap values for TiO_2 and TiO_2:Ag samples were 3.03 and 1.52 eV, respectively. The exponential optical absorption edge, and hence the optical band gap, is controlled by the degree of structural order/disorder of the TiO_2 or TiO_2:Ag lattice, interface, and surface.

The decrease in the band gap can be directly related to the increase in defects in the TiO_2 lattice. In this study, the modification of the TiO_2 lattice induced by Ag recovery raised the intermediary levels within the band-gap region, thus reducing the measured optical band gap. Increased disorder is linked to deep defects within the band gap and increased order is associated with shallow defects that readily disappear if total order is achieved.

The tail of the absorbance spectrum trace observed for TiO_2:Ag samples indicates the presence of several new states; hence, localized electronic levels in the forbidden band gap are probably introduced by the presence of metallic Ag [33]. The drastic reduction in the band gap of TiO_2:Ag could occur by virtue of a plasmonic effect of Ag on the surface, the presence of this new structure on the surface creating new localized levels in the band gap, or, most probably, both. In plasmonics, metal nanostructures can serve as antennae to convert light into localized electric fields or as waveguides to route light to desired locations with nanometer precision [34]. With a tight control over the nanostructures in terms of size and shape, light can be effectively manipulated and controlled with unprecedented accuracy [35]. Of all metals, Ag has played the most important role in the development of plasmonics, and its unique properties make it well suited for most next-generation plasmonic technologies. The plasmonic surface is unique, in that it can use nanostructures of different sizes (from tens to hundreds of nanometers), thus bridging the gap between the micrometer and nanometer levels.

These results indicate that the heterostructure formed with TiO_2 and Ag increased the formation of deep states in the band gap, leading to electron sharing between TiO_2 and Ag
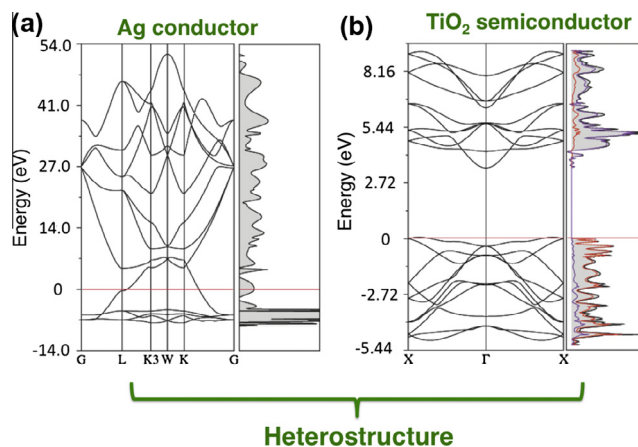
(semiconductor/metal). Theoretical models are very useful in rendering an interesting perception of the effects of diverse structural modifications to the electronic structure, and consequently the band gap, of a material. This is useful in the present case for improved understanding of the overall process.

Fig. 3 depicts the band structure and projected DOS of TiO_2 and Ag; we can observe how the electronic structures of TiO_2 and of Ag are aligned, and observe the atomic-level interaction between TiO_2 and Ag in the heterostructure. This is a useful way to represent interfaces and was previously used by our group to model the bulk/surface structure of TiO_2 [24] and a Ag_2WO_4:Ag heterostructure [25].

The calculated indirect band gap, between the X-point in the valence band and the Γ-point in the conduction band (CB) of the irreducible Brillouin zone, for the anatase phase was 3.51 eV. As expected, the band structure of the Ag phase had a characteristic metallic profile. The TiO_2 and Ag phases each showed a local far-field interaction in their band gap, which probably facilitated hybridization between the TiO_2 and metallic Ag band gaps, and resulted in a total reduction of 1.51 eV for the experimentally measured total band gap.

The FEG-SEM micrograph shows that TiO_2:Ag structures have an apparent homogenous and spherical morphology (Fig. 4a and b), with an agglomerate and polydisperse nature.

As can be seen in Fig. 4, the random aggregation process between the small spherical TiO_2:Ag nanoparticles resulted in a shapeless grain morphology. The HTMW route for synthesizing nanoparticles, the focus of a rapidly developing area of research, has been shown to be efficient in the processing of several complex oxides [36]. Bilecka and Niederberger [37] have published an overview of microwave-assisted liquid-phase routes for the preparation of inorganic nanomaterials. When synthesizing nanoparticles from a solution (or a gas phase), the growth of an individual nanostructure following the nucleation process occurs by two primary mechanisms: aggregation and coarsening. Crystal growth by aggregation may occur via a range of mechanisms, including interaction between randomly oriented particles (coalescence) or highly oriented particles (oriented attachment). Coalescence is defined as aggregation of two nanoparticles of roughly equal size, with no molecular exchange between them [38]. The oriented attachment mechanism is based on the assumption that nanoparticles dispersed in a liquid medium possess a very high degree of freedom for rotational and translational motion, when coalescence does not take place; in fact, crystal growth occurs by means of oriented collisions/rotation and is called non-classical crystallization [39]. In the present study, the morphology of the TiO_2:Ag nanopar-
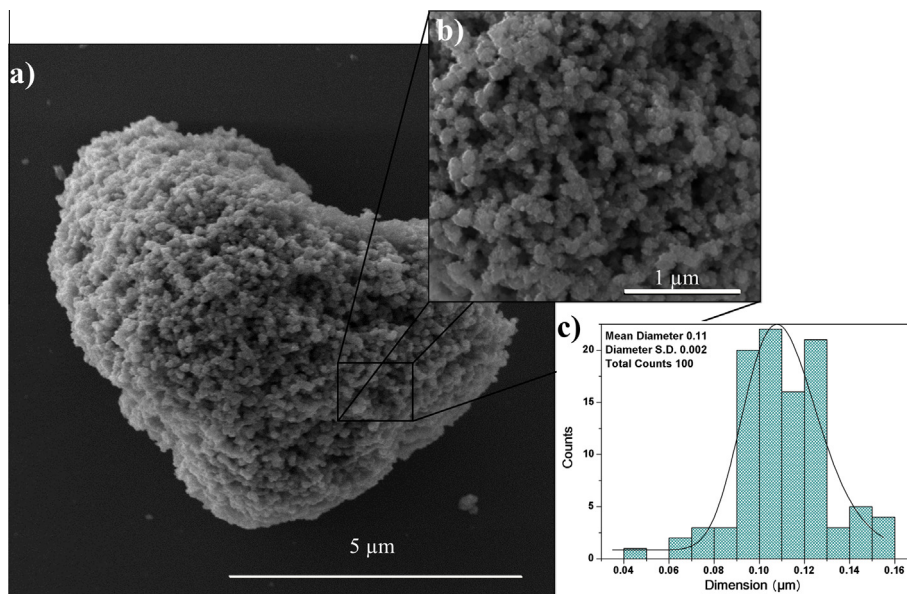
Fig. 4. (a) FEG-SEM micrograph of TiO_2:Ag nanoparticles; (b) magnified view of the FEG-SEM micrograph; (c) size-distribution histogram indicating the mean sizes for a total of 100 nanoparticles.

ticle seems to result from the aggregation mechanism. The facility and low-temperature requirements for the synthesis of TiO_2:Ag nanoparticles were attributed to the rapid rate of the reaction and direct microwave coupling with a water rotational barrier, which allowed uniform heating of the solution at start-up [40]. Compared with the usual methods, HTMW has the advantages of shortening the reaction time and producing products with a small particle size, narrow particle-size distribution, and high purity. However, the exact nature of the interaction of microwaves with reactants during particle synthesis is somewhat unclear and spec-ulative, although the interaction of dielectric materials, liquids, or solids, with microwaves leads to a phenomenon commonly known as dielectric heating. However, its aforementioned characteristics qualify HTMW as a typical bottom-up process. The average nanocrystal particle-size distribution was estimated from FEG-SEM micrographs by analysis of 100 particles with a mean diameter of 112 nm (Fig. 2c), using the ImageJ software [41].

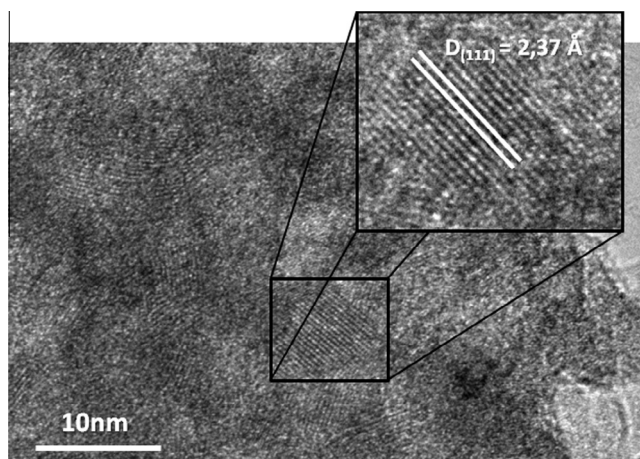HRTEM micrographic analysis (Fig. 5) showed spherical nanoparticles homogeneously distributed on the TiO_2 surface.

These nanoparticles, with diameters of <10 nm, were identified as metallic Ag with an interplanar distance of 2.37 Å, which corre-sponded to the (1 1 1) plane of Ag, according to the XRD pattern (PDF 65-2871; see Fig. 3). This result confirms the presence of Ag on the TiO_2 surface, showing the impregnation of TiO_2 with metal-lic Ag to form a heterostructure. Observation of the HRTEM image (Fig. 5, inset) confirms that the TiO_2:Ag nanoparticles were formed by interactions between randomly oriented TiO_2 and Ag particles, namely, coalescence (see Fig. 6).

The short-range order of TiO_2 and TiO_2:Ag samples was investi-gated by FT-Raman analysis. All Raman modes observed for the TiO_2 sample were attributed to the anatase phase, with peaks cen-tered at 149, 200, 402, 518, and 642 cm^{-1} being related to the five Raman-active modes with the symmetries $E_{g(1)}$, $E_{g(2)}$, $B_{1g(3)}$, $A_{1g(4)}$, and $E_{g(3)}$, respectively [24,42]. As recently reported from theoreti-cal calculations, 518 cm^{-1} corresponds to a B_{1g} Raman-active mode [21].

The TiO_2:Ag Raman spectra showed a shift in the frequency of Raman-active modes that can be attributed to the local disorder

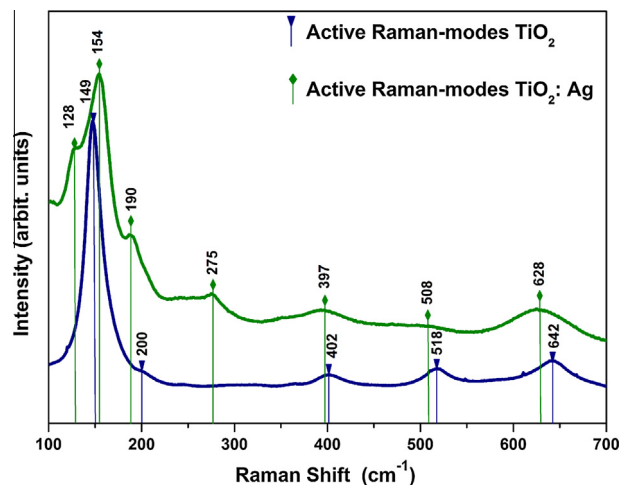**Fig. 5.** High-resolution transmission electron microscopy image of a TiO_2 nano-sphere with Ag impregnation. The interplanar distance of 2.37 Å corresponds to the (1 1 1) plane of Ag (inset).

Fig. 6. Fourier transform-Raman spectra for TiO_2 and TiO_2:Ag, as recorded at room temperature.

caused by the addition of Ag on the surface of TiO_2. In addition, the TiO_2:Ag sample presented two uncharacteristic anatase Raman-active modes at 128 and 275 cm^{-1}. These Raman modes are very close to those presented by the brookite phase of TiO_2 [43,44]. The appearance of the latter phase could be due to a compressive stress on the first few layers of TiO_2 molecules that packs the surface atoms closely because of the presence of Ag on the surface. This compressive force could be responsible for an induced phase-transformation from the anatase to brookite phase of TiO_2. The long-range XRD analysis of TiO_2:Ag did not detect the brookite phase of TiO_2, probably because of its low content.

Additional evidence of a compressive force at the TiO_2:Ag heterostructure surface is the $E_{g(1)}$ (154 cm^{-1}) and $E_{g(2)}$ (190 cm^{-1}) inelastic modes that demonstrate a blue shift and red shift, respectively, when compared with the TiO_2 sample. A pressure effect induced by the surrounding particles and interface stress in lead titanate ($PbTiO_3$) nanocrystals was successfully used to induce a frequency shift of the soft mode at 89 cm^{-1} [45,46]. Saviot et al. [46] reported experimental and theoretical results showing that $E_{g(1)}$ and $E_{g(2)}$ frequencies for bulk anatase under hydrostatic pressure cannot be degenerate, and an anti-crossing pattern must exist. In other words, when the anatase phase was submitted to a pressure of <7 GPa, the intensity of the $E_{g(1)}$ frequency showed a blue shift, and that of $E_{g(2)}$ a red shift. This anti-crossing behavior is rather well reproduced in the calculations reported by Albuquerque et al. [19].

The MIC values obtained for TiO_2:Ag against the planktonic strains of *C. albicans*, *C. glabrata*, and *C. tropicalis* were 62.5, 15.0, and 31.25 mg L^{-1}, respectively, showing that *C. glabrata* was the most susceptible species, while *C. albicans* was the most resistant. Other studies also found that the MIC values for both Ag and gold nanoparticles differed for different *Candida* spp., as well as between clinical isolates and reference strains [47,48]. Despite different levels of susceptibility, TiO_2:Ag nanoparticles were able to inhibit the growth of three *Candida* spp. In a previous study, microbiological tests showed that the exposure of *C. albicans* to anatase TiO_2 nanoparticles did not completely inhibit its growth (only a 30% reduction was reported) [24]; these findings confirm one of the advantages of using TiO_2 and Ag in association. Additionally, at concentrations of >250 mg L^{-1} TiO_2:Ag, the $\log_{10}(CFU\ mL^{-1})$ value was zero for *C. glabrata* (MFC = 250 mg L^{-1}), indicating that the TiO_2:Ag nanoparticles were able to kill *C. glabrata* planktonic cells. Although no MFC value was obtained for the other two *Candida* spp., there were significant reductions in the $\log_{10}(CFU/mL)$ values for *C. albicans* and *C. tropicalis* treated with TiO_2:Ag at concentrations of >125 and 31.25 mg L^{-1}, respectively (Fig. 7). Although the MIC values of Ag nanoparticles obtained in other studies [49,50] were lower than those obtained in the present study, it is important to highlight that a hybrid nanomaterial was used in this case. Another study also evaluated a hybrid nanomaterial, Ag-decorated hydroxyapatite (HA@Ag), and reported MIC and MFC values of 62.5 and 250 mg L^{-1}, respectively, for *C. albicans*, similar to the values obtained in the present study [16]. Combining nanoparticles reduces the concentration of each individual nanoparticle. Therefore, during Ag impregnation of TiO_2 in the present study, 7×10^{-5} mol $AgNO_3$ could achieve an Ag/Ti ratio of 0.06 in the resultant TiO_2:Ag. Reduced concentration of Ag is of interest, as it may decrease both the cost of manufacturing and the cytotoxicity to host cells, in addition to preventing microbial resistance.

Antimicrobial tests using planktonic MRSA cells yielded MIC and MBC values of 500 and 1000 mg L^{-1} TiO_2:Ag, respectively, indicating bacteriostatic and bactericidal effects. These results are partly in agreement with those reported by Kowal et al. [51], who obtained MICs for MRSA cells, but not for *C. albicans*, when amorphous states of Ag-doped Ti were used without UV irradiation. However, inhibition of cell growth was not observed when
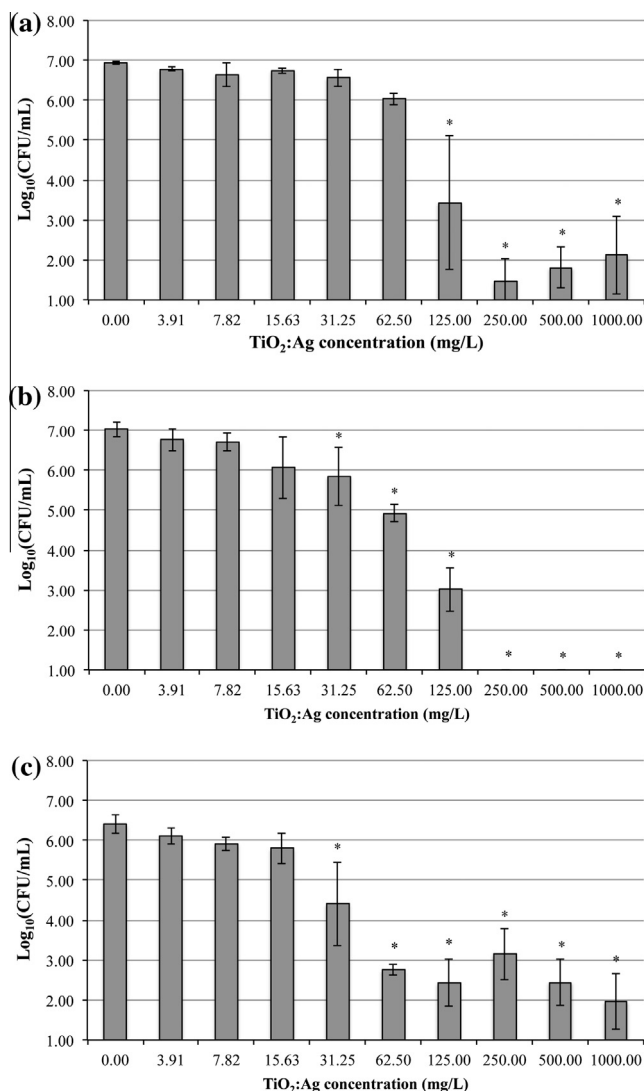

Fig. 7. Mean values of $\log_{10}(CFU\ mL^{-1})$ of (a) *Candida albicans*, (b) *C. glabrata*, and (c) *C. tropicalis*) planktonic cells after incubation with serial two-fold dilutions of TiO_2:Ag ($\mu g\ mL^{-1}$) in RPMI-1640 medium. Error bars represent standard deviation. *: Significantly different from 0 (control), 15.62, 31.25, 62.5, 125, and 250 $\mu g\ mL^{-1}$.

non-irradiated Ag-doped crystalline anatase was evaluated. This was attributed to an increase in the size of the Ag particles and their reduced content at the crystal surface. The size and shape of nanoparticles, the nature of support materials, and the components of nanocomposites may influence the antimicrobial activity of nanomaterials. Smaller particles can interact more efficiently with the bacterial surface and penetrate into the cell [52]. Potara et al. [9] suggested that an increased uptake rate of smaller particles could also increase the intracellular release of Ag ions, which might add to the antimicrobial effect. In the present study, the size of the Ag nanoparticles decorating the TiO_2 surface was very small (<10 nm), which may have contributed to the antibacterial effect against the methicillin-resistant strain of *S. aureus*.

When biofilms were cultivated, no MFCb was obtained for any of the *Candida* spp. studied, i.e., no concentration of TiO_2:Ag was found to completely inhibit the growth of *C. albicans*, *C. glabrata*, or *C. tropicalis*. Nonetheless, significant reductions, of 2.11, 1.54, and 1.64 $\log_{10}(CFU\ mL^{-1})$, were observed for treatment of *C. albicans*, *C. glabrata*, and *C. tropicalis* biofilms, respectively, with 1000 mg L^{-1} TiO_2:Ag (data not shown). Similarly, for MRSA, no MBCb was obtained for TiO_2:Ag, i.e., no concentration of TiO_2:Ag

was found to completely inhibit growth of MRSA biofilms. However, the mean $\log_{10}$(CFU mL^{-1}) values of MRSA biofilms obtained at 500 and 1000 mg L^{-1} TiO$_2$:Ag were significantly lower ($P < 0.05$) compared with those of the control culture, with reductions of 2.33 and 1.81 $\log_{10}$(CFU mL^{-1}), respectively (data not shown). As expected, the antimicrobial activity of the TiO$_2$:Ag nanoparticles against biofilm-forming cells was lower than that against planktonic cultures. This result is in agreement with that reported by Zamperini al. [16], who also observed that reduction of $\log_{10}$(CFU mL^{-1}) values of *C. albicans* biofilms was only achieved with HA@Ag at 1000 mg L^{-1}. Resistance to Ag nanoparticles exhibited by biofilm cells has been demonstrated in recent studies [23]. Even when Ag nanoparticles were combined with nystatin or chlorhexidine, only a synergic or additive effect was observed for biofilms of *C. albicans* and *C. glabrata*, without complete biofilm eradication by any Ag/drug combination. Among other factors, the presence of extracellular polymeric matrix among biofilm-forming cells probably impairs the diffusion of metal nanoparticles and, consequently, inhibits direct contact between them and the cells present in the deeper layers of the biofilm. Other factors that have been associated with the drug resistance exhibited by biofilm cells include lower growth rate, heterogeneity, gene expression related to drug resistance, and the presence of persistent cells [10].

Crystal violet staining also demonstrated a significant reduction ($P < 0.05$) in the total biomass (lower absorbance values) of *Candida* spp. and MRSA biofilms treated with 1,000 mg L^{-1} TiO$_2$:Ag. Reductions of 35.66%, 20.70%, and 19.51% for *C. albicans*, *C. glabrata*, and *C. tropicalis*, respectively, and 11.91% for MRSA, were observed (data not shown); these results are in agreement with those obtained from the viability assay (CFU mL^{-1}). Previous studies also demonstrated a reduction of the biofilm biomass of *Candida* spp. treated with HA@Ag [16] and Ag nanoparticles [10]. However, few studies have evaluated the antimicrobial effect of nanoparticles against MRSA biofilms. A recent investigation showed that treatment with Ag-conjugated, superparamagnetic iron oxide nanoparticles at a concentration of 1 mg mL^{-1} resulted in a 30% reduction of the MRSA biofilm biomass, as evaluated by crystal violet staining [53]. A decrease in biofilm biomass indicated that TiO$_2$:Ag nanoparticles can disrupt biofilms. This is an important finding, because when a biofilm is dispersed and cells become detached, the susceptibility of cells to antimicrobial agents is higher than that of cells within an intact biofilm.

To understand the role of the metal:oxide interaction, we analyzed the electronic structure and Fermi level of both Ag and TiO$_2$. Fig. 8 shows the comparative DOSs of Ag and TiO$_2$.

As shown in Fig. 8, Ag shows several electronic states in the region of the TiO$_2$ band gap. When Ag was used to decorate TiO$_2$, in the TiO$_2$:Ag heterostructure obtained in the present study, the metal may have filled some electronic bands of the semiconductor, decreasing the band gap of the system. As a result, the metal may inject electrons into the TiO$_2$, creating holes on the TiO$_2$ surface.

Fig. 9 shows the TiO$_2$:Ag heterostructure model, [Ag]$_4$/TiO$_{2-x}$ with the electronic spin density isosurface, located around the metal clusters. It is also showed the band structure and the projected DOS. In this case its clear that the intermediary levels are attributed for the absorbed [Ag$_4$] cluster. It is expected that the number of ney levels in the gap increases with the cluster size. For nanostructured materials, discrete levels with high Fermi level and high strained clusters are more reactive than extended surfaces.

We can observe that this model are consistent with the previously one presented here noted by the similarity between the band structure and projected DOS. However in the first case the computational cust is smaller.

The TiO$_2$:Ag semiconductor–metal heterostructure is a good example of space-charge layers, band bending, and formation of
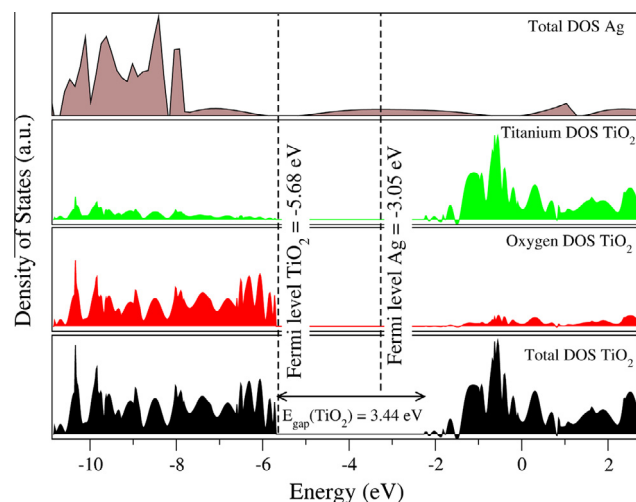

Fig. 8. Projected total density of states of TiO$_2$ and metallic Ag, and projected atomic states with regard to oxygen and titanium in TiO$_2$.

a Schottky barrier, as shown in Fig. 10. Electrically neutral and isolated from each other, the metal and the semiconductor have different Fermi level positions. As seen with the heterostructure obtained in the present study, the metal has a higher Fermi level position than the semiconductor. When the two materials are electrically connected, electron migration from the semiconductor to the metal occurs until the two Fermi levels are aligned, as shown in Fig. 10. The electrical contact thus forms a space-charge layer. The surface of the metal acquires excess negative charge, while the semiconductor exhibits excess positive charge, because of the migration of an electron from the barrier region; the electronic bands of the semiconductor bend upward, toward its surface, and the space-charge layer is said to be depleted. The barrier formed at the metal:semiconductor interface is termed the Schottky barrier. The diagram in Fig. 10 illustrates an ideal metal:semiconductor contact, i.e., no surface states exist on the semiconductor. The Schottky barrier produced at the metal:semiconductor interface can serve as an efficient electron trap, preventing electron–hole recombination [54].

In nanoparticles, oxygen vacancies can function as a point defect and are present in three different charge states: neutral oxygen vacancy (V_O^x), singly occupied oxygen vacancy (V_O^x), and doubly occupied ($V_O^{\bullet\bullet}$) states. It can be inferred that increased disorder in the lattice is associated with the presence of $[TiO_5 \cdot V_O^x]$, $[TiO_5 \cdot V_O^{\bullet}]$, and $[TiO_5 \cdot V_O^{\bullet\bullet}]$ complex clusters, and that these complex defects are shallow and/or deeply inserted in the band gap [24].

Clusters of Ag nanoparticles exhibit collective oscillation of their electrons in the CB, which is known as localized surface plasmon resonance. The complex defects of TiO$_2$ allow interactions with the $[Ag_4]^x$ clusters of Ag nanoparticles, i.e., an association between the semiconductor and the metal plasmon [52]. The association between the semiconductor and metal changes the effectiveness and mechanism of antimicrobial activity of each.

In the model proposed here, the most important events occur at the interface of the plasmon and semiconductor. This involves an electron-transfer process at the metal:semiconductor interface, with the formation of superoxide, hydrogen ions (H$^+$), and/or OOH* radicals by electron–hole reactions, which causes protein inactivation and eventual apoptosis [16]. Moreover, an effective charge separation exists between the TiO$_2$ bulk and surface, and the metal at the semiconductor surface is able to conduct these charges to the solution.
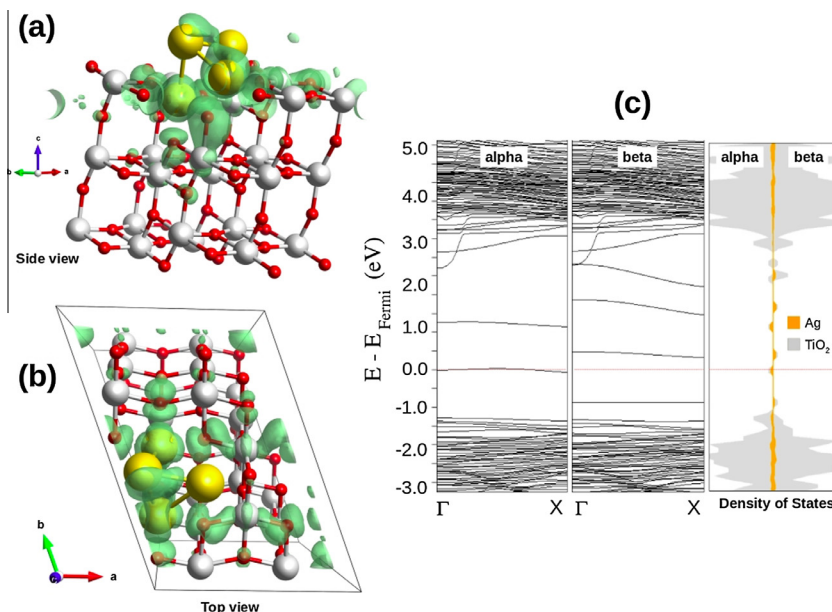
Fig. 9. (a) Side view, (b) top view of [Ag$_4$] cluster adsorbed on reduced TiO$_{2-x}$ (101) surface with the electronic spin density isosurface (green surface; isovalue 0.001 e/Å^3) at the topmost layers of the heterostructure around [Ag$_4$] cluster, and (c) band structure and DOS shown the appearance of intermediary levels at the TiO$_2$ gap by the adsorbed silver atoms. The silver, titanium and oxygen atoms are shown in yellow, white and red, respectively. (For interpretation of the references to colour in this figure legend, the reader is referred to the web version of this article.)
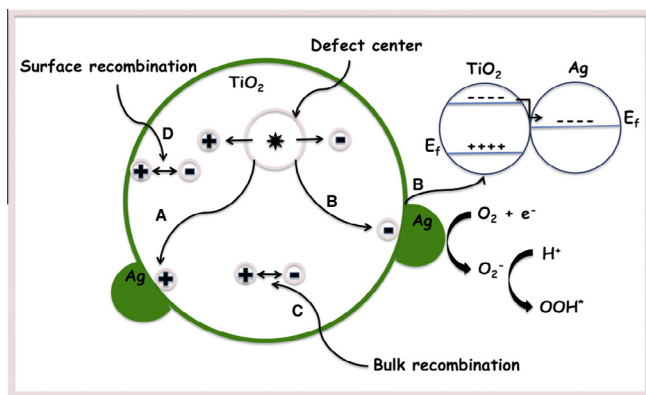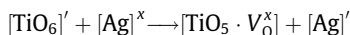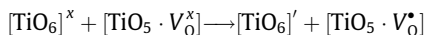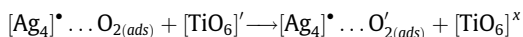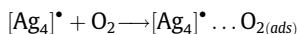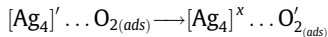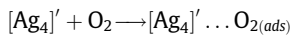

Fig. 10. Possible mechanisms in the heterostructure formed by TiO$_2$ and Ag nanoparticles. (a) Hole trap at the surface; (b) electron conduction by the Ag nanoparticle; (c) bulk recombination; (d) surface recombination.

Consequently, the effect of surface properties on the electron–hole reaction performance should be considered in terms of the following:

$$[TiO_6]^x + [TiO_5 \cdot V_O^x] \longrightarrow [TiO_6]' + [TiO_5 \cdot V_O^\bullet]$$

$$[TiO_6]' + [Ag]^x \longrightarrow [TiO_5 \cdot V_O^x] + [Ag]'$$

The reactivity of molecular oxygen with a complex [Ag]' on the Ag surface results in a chemisorbed species and subsequent oxygen incorporation into the lattice:

$$[Ag_4]' + O_2 \longrightarrow [Ag_4]' \ldots O_{2(ads)}$$

$$[Ag_4]' \ldots O_{2(ads)} \longrightarrow [Ag_4]^x \ldots O'_{2(ads)}$$

$$[Ag_4]^\bullet + O_2 \longrightarrow [Ag_4]^\bullet \ldots O_{2(ads)}$$

$$[Ag_4]^\bullet \ldots O_{2(ads)} + [TiO_6]' \longrightarrow [Ag_4]^\bullet \ldots O'_{2(ads)} + [TiO_6]^x$$

The clusters formed by the Ag complex also interact with H$^+$ and split into peroxide oxygen according to the following reaction:

$$[Ag_4]^x \ldots O'_{2(ads)} + H^+ \longrightarrow [OOH]^*$$
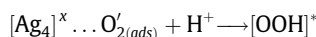
The HO$_2^*$ radical may react with microbial cells, ultimately resulting in the oxidation of cellular components. Therefore, even with an agglomerate morphology, nanoparticles exhibit antimicrobial activity due to their physicochemical property of oxidation.

5. Conclusions

An Ag nanoparticle-coated TiO$_2$ heterostructure was synthesized using the safe, ecofriendly, and reproducible HTMW method. These nanoparticles exhibited physicochemical properties that conferred antimicrobial activity against planktonic and biofilm-forming cells of MRSA and *Candida* spp. Biofilm-forming strains showed increased tolerance compared to planktonic strains. To the best of our knowledge, this is the first report on the effect of TiO$_2$:Ag nanoparticles, produced via HTMW, on *Candida* spp. and MRSA biofilms. Moreover, the mechanism underlying the antimicrobial activity of TiO$_2$:Ag nanoparticles is suggested on the basis of theoretical calculations.

Conflict of interest

No conflict of interest.

Acknowledgments

References

[1] A.Y. Zhang, M.H. Zhou, L. Han, Q.X. Zhou, J. Hazard. Mater. 186 (2011) 1374.
[2] C. Botta, J. Labille, M. Auffan, D. Borschneck, H. Miche, M. Cabie, A. Masion, J. Rose, J.Y. Bottero, Environ. Pollut. 159 (2011) 1543.

[3] H.J. Yun, H. Lee, J.B. Joo, N.D. Kim, J. Yi, J. Nanosci. Nanotechnol. 11 (2011) 1688.

[4] W.Q. Peng, M. Yanagida, L.Y. Han, S. Ahmed, Nanotechnology 22 (2011).

[5] W.S. Tung, W.A. Daoud, J. Mater. Chem. 21 (2011) 7858.

[6] A. Fujishima, K. Honda, Nature 238 (1972) 37.

[7] F. Haghighi, S.R. Mohammadi, P. Mohammadi, M. Eskandari, S. Hosseinkhani, Med. J. 113 (2012) 707.

[8] R.G. Nair, J.K. Roy, S.K. Samdarshi, A.K. Mukherjee, Colloid Surf. B Biointerfaces 86 (2011) 7.

[9] M. Potara, E. Jakab, A. Damert, O. Popescu, V. Canpean, S. Astilean, Nanotechnology 22 (2011).

[10] A. Bokare, A. Sanap, M. Pai, S. Sabharwal, A.A. Athawale, Colloid Surf. B Biointerfaces 102 (2013) 273.

[11] P.V. Sanita, A.C. Pavarina, E.T. Giampaolo, M.M. Silva, E.G. de Oliveira Mima, D.G. Ribeiro, C.E. Vergani, Oral Surg. Oral Med. Oral Pathol. Oral Radiol. Endodontol. 111 (2011) 726.

[12] V. Krcmery, A.J. Barnes, J. Hosp. Infect. 50 (2002) 243.

[13] I.M. Gould, M.Z. David, S. Esposito, J. Garau, G. Lina, T. Mazzei, G. Peters, Int. J. Antimicrob. Agents 39 (2012) 96.

[14] I. Perelshtein, G. Applerot, N. Perkas, J. Grinblat, A. Gedanken, Chem. Eur. J. 18 (2012) 4575.

[15] N. Hoiby, T. Bjarnsholt, M. Givskov, S. Molin, O. Ciofu, Int. J. Antimicrob. Agents 35 (2010) 322.

[16] C.A. Zamperini, R.S. Andre, V.M. Longo, E.G. Mima, C.E. Vergani, A.L. Machado, J.A. Varela, E. Longo, J. Nanomater. (2013).

[17] A.s.M.-A. National Committee for Clinical Laboratory Standards: Methods for Dilution Antimicrobial Susceptibility Tests for Bacteria That Grow Aerobically, NCCLS, seventh ed. (Ed.), Wayne, PA, USA, 2006.

[18] A.S. Clinical and Laboratory Standards Institute: Reference Method for Broth Dilution Antifungal Susceptibility Testing of Yeasts, CLSI Document M27-A3, third ed. (Ed.), Wayne, PA, 2008.

[19] A.R. Albuquerque, J. Maul, E. Longo, I.M.G. dos Santos, J.R. Sambrano, J. Phys. Chem. C 117 (2013) 7050.

[20] A.R. Albuquerque, I.M.G. Santos, J.R. Sambrano, Quim. Nova 37 (2014) 1318.

[21] A.D.R. Albuquerque, M.L. Garzim, I.M.G.D. Santos, V. Longo, E. Longo, J.R. Sambrano, J. Phys. Chem. A 116 (2012) 11731–11735.

[22] A.R. Albuquerque, A. Bruix, I.M.G. dos Santos, J.R. Sambrano, F. Illas, J. Phys. Chem. C 118 (2014) 9677.

[23] C.W. Raubach, Y.V.B. de Santana, M.M. Ferrer, V.M. Longo, J.A. Varela, W. Avansi, P.G.C. Buzolin, J.R. Sambrano, E. Longo, Chem. Phys. Lett. 536 (2012) 96.

[24] V.M. Longo, F.C. Picon, C. Zamperini, A.R. Albuquerque, J.R. Sambrano, C.E. Vergani, A.L. Machado, J. Andres, A.C. Hernandes, J.A. Varela, E. Longo, Chem. Phys. Lett. 577 (2013) 114.

[25] V.M. Longo, C.C. De Foggi, M.M. Ferrer, A.F. Gouveia, R.S. Andre, W. Avansi, C.E. Vergani, A.L. Machado, J. Andres, L.S. Cavalcante, A.C. Hernandes, E. Longo, J. Phys. Chem. A 118 (2014) 5769.

[26] R. Dovesi, V.R. Saunders, C. Roetti, R. Orlando, C.M. Zicovich-Wilson, F. Pascale, B. Civalleri, K. Doll, N.M. Harrison, I.J. Bush, P. D'Arco, M. Llunell, M. Causà, Y. Noël, CRYSTAL14 User's Manual, University of Torino, Torino, 2014.

[27] H.P. Hratchian, A.V. Krukau, P.V. Parandekar, M.J. Frisch, K. Raghavachari, J. Chem. Phys. 136 (2012).

[28] M.L. Moreira, E.C. Paris, Acta Mater. 57 (2009) 5174.

[29] M.L. Moreira, J. Andres, J.A. Varela, E. Longo, Cryst. Growth Des. 9 (2009) 833.

[30] V.M. Longo, L.S. Cavalcante, E.C. Paris, J.C. Sczancoski, P.S. Pizani, M.S. Li, J. Andres, E. Longo, J.A. Varela, J. Phys. Chem. C 115 (2011) 5207.

[31] M.L. Moreira, P.G.C. Buzolin, V.M. Longo, N.H. Nicoleti, J.R. Sambrano, M.S. Li, J.A. Varela, E. Longo, J. Phys. Chem. A 115 (2011) 4482.

[32] D.L. Wood, J. Tauc, Phys. Rev. B 5 (1972) 3144.

[33] V.M. Longo, L.S. Cavalcante, R. Erlo, V.R. Mastelaro, A.T. de Figueiredo, J.R. Sambrano, S. de Lazaro, A.Z. Freitas, L. Gomes, N.D. Vieira, J.A. Varela, E. Longo, Acta Mater. 56 (2008) 2191.

[34] M. Rycenga, C.M. Cobley, J. Zeng, W. Li, C.H. Moran, Q. Zhang, D. Qin, Y. Xia, Chem. Rev. 111 (2011) 3669.

[35] M.L. Brongersma, V.M. Shalaev, Science 328 (2010) 440.

[36] D.P. Volanti, D. Keyson, L.S. Cavalcante, A.Z. Simoes, M.R. Joya, E. Longo, J.A. Varela, P.S. Pizani, A.G. Souza, J. Alloys Compd. 459 (2008) 537.

[37] I. Bilecka, M. Niederberger, Nanoscale 2 (2010) 1358.

[38] M. Jose-Yacaman, C. Gutierrez-Wing, M. Miki, D.Q. Yang, K.N. Piyakis, E. Sacher, J. Phys. Chem. B 109 (2005) 9703.

[39] H.C. Zeng, Int. J. Nanotechnol. 4 (2007) 329.

[40] G.J. Wilson, A.S. Matijasevich, D.R.G. Mitchell, J.C. Schulz, G.D. Will, Langmuir 22 (2006) 2016.

[41] <http://rsbweb.nih.gov/ij/>.

[42] K.M. Rahulan, N. Padmanathan, L.D. Stephen, C.C. Kanakam, J. Alloys Compd. 554 (2013) 432.

[43] M.N. Iliev, V.G. Hadjiev, A.P. Litvinchuk, Vib. Spectrosc. 64 (2013) 148.

[44] G.A. Tompsett, G.A. Bowmaker, R.P. Cooney, J.B. Metson, K.A. Rodgers, J.M. Seakins, J. Raman Spectrosc. 26 (1995) 57.

[45] J.F. Meng, G.T. Zou, Q.L. Ciu, Y.N. Zhao, Z.Q. Zhu, J. Phys. Condens. Matter 6 (1994) 6543.

[46] L. Saviot, D. Machon, L. Debbichi, A. Girard, J. Margueritat, P. Krueger, M.C.M. de Lucas, A. Mermet, J. Phys. Chem. C 118 (2014) 10495.

[47] A. Jebali, F.H.E. Hajjar, F. Pourdanesh, S. Hekmatimoghaddam, B. Kazemi, A. Masoudi, K. Daliri, N. Sedighi, Med. Mycol. 52 (2014) 65.

[48] K.-J. Kim, W.S. Sung, S.-K. Moon, J.-S. Choi, J.G. Kim, D.G. Lee, J. Microbiol. Biotechnol. 18 (2008) 1482.

[49] D.R. Monteiro, S. Silva, M. Negri, L.F. Gorup, E.R. de Camargo, R. Oliveira, D.B. Barbosa, M. Henriques, Mycoses 56 (2013) 672.

[50] A. Panacek, L. Kvitek, R. Prucek, M. Kolar, R. Vecerova, N. Pizurova, V.K. Sharma, T. Nevecna, R. Zboril, J. Phys. Chem. B 110 (2006) 16248.

[51] K. Kowal, K. Wysocka-Krol, M. Kopaczynska, E. Dworniczek, R. Franiczek, M. Wawrzynska, M. Vargova, M. Zahoran, E. Rakovsky, P. Kus, G. Plesch, A. Plecenik, F. Laffir, S.A.M. Tofail, H. Podbielska, J. Colloid Interface Sci. 362 (2011) 50.

[52] J.R. Morones, J.L. Elechiguerra, A. Camacho, K. Holt, J.B. Kouri, J.T. Ramirez, M.J. Yacaman, Nanotechnology 16 (2005) 2346.

[53] N.G. Durmus, T.J. Webster, Adv. Healthcare Mater. 2 (2013) 165.

[54] A.L. Linsebigler, G.Q. Lu, J.T. Yates, Chem. Rev. 95 (1995) 735.